

Double-Sided Design of Electrodes Driving Tunable Dielectrophoretic Miniature Lens

Yousuf D. Almoallem and Hongrui Jiang, *Fellow, IEEE*

Abstract—We demonstrate the design methodology, geometrical analysis, device fabrication, and testing of a double-sided design of tunable-focus dielectrophoretic liquid miniature lenses. This design is intended to reduce the driving voltage for tuning the lens, utilizing a double-sided electrode design that enhances the electric field magnitude. Fabricated devices were tested and measurements on a goniometer showed changes of up to 14° in the contact angle when the dielectrophoretic force was applied under $25 V_{\text{rms}}$. Correspondingly, the back focal length of the liquid lens changed from 67.1 to 14.4 mm when the driving voltage was increased from 0 to $25 V_{\text{rms}}$. The driving voltage was significantly lower than those previously reported with similar device dimensions using single-sided electrode designs. This design allows for a range of both positive and negative menisci dependent on the volume of the lens liquid initially dispensed. [2017-0011]

Index Terms—Miniature lens, tunable lens, dielectrophoretic, microelectromechanical systems (MEMS) actuator, optofluidics, electrohydrodynamic.

I. INTRODUCTION

MINIATURIZING camera systems as required in many new compact devices places a severe restriction on the device size and power consumption. Tunable miniature lenses overcome aforementioned concerns and present a viable solution by tuning the focal length of lenses via, for example, variation in the lens curvature. The understanding of the balance of forces at the liquid-phase boundaries has solved a bottleneck issue in the field of tunable liquid lenses. Indeed, it has opened the door for many applications of wetting phenomena, capillary forces, contact angle formation, etc. [1]. The influence of interfacial tension as a key metric in controlling a fluid system has drawn considerable attention in biomedical, industrial, military fields over the past decade [2]–[4]. In optofluidics, appropriate material selection and scaling

of device design establish a tuned environment with proper energy balance at the phase boundaries, which in turn allows for the tuning of the miniature lens profile with reasonable external forces. This allows manufacturers to vary the focal length of the lens itself, rather than mechanically varying the distances between the lenses, as in the traditional situation.

Tunable-focus lenses can be classified into two categories based on the variable being adapted, i.e. the refractive index or the profile curvature. The first category covers the gradient-index lenses, where, as an example, liquid crystals permit the variation of the refractive index by reorientation of the liquid crystal molecules under an electric field. However, they tend to have relatively large optical aberrations caused by the birefringence effect as discussed in [5] and [6]. In the second category, the lens profile can be reshaped through various mechanisms with or without an elastic membrane. Some examples of actuation are fluidic (pneumatic) pressure [7], thermal [8], stimuli-responsive hydrogel [1], [9], ferrofluidic piston [10], acoustic waves [11], electrowetting [12]–[14], and dielectrophoretic (DEP) [15]–[17]. The electrowetting and the dielectric mechanisms are sometimes referred to as electrohydrodynamic actuations. Both are especially promising since they have the capability to achieve a faster response. Above all, dielectric lenses overcome the electrolysis issue encountered in electrowetting lenses [15]–[17]. Both mechanisms, nonetheless, usually require high voltage levels exceeding $100 V_{\text{rms}}$ or even reaching $200 V_{\text{rms}}$ as in [15]–[24]. Some efforts were directed towards overcoming this barrier as reported in [25]–[27]. Nevertheless, the driving voltage in these designs was still high and could lead to other issues such as restricted focus tuning range.

In this paper, we report on a tunable dielectric liquid lens with a double-sided electrode design, unlike in the conventional scheme with a single-sided electrode design. The proposed design significantly enhances the magnitude of the actuation electric field, $|\vec{E}|$. Therefore, the driving voltage is much reduced and the required DEP force is generated by both sets of the double-sided electrodes. In this work, we employed the dielectric actuation mechanism for our liquid lens. The same concept can be readily extended to electrowetting-based actuation.

II. METHODS

A. Device Design Principle

The idea of the presented work is based on dielectrophoretic (DEP) tunable miniature lenses operating at relatively low voltage levels. Such a miniature lens comprises of two immiscible liquids: the first being polar, while the second non-polar. A non-uniform electric field creates a dielectric

Manuscript received January 15, 2017; revised May 15, 2017; accepted May 29, 2017. Date of publication June 13, 2017; date of current version September 29, 2017. This work was supported in part by the U.S. National Science Foundation under Grant CNS 1329481, and in part by the U.S. National Institutes of Health under Grant 1DP2OD008678-01 and Grant 5R01EB019460-02. The work of Y. Almoallem was supported by the Saudi Government Scholarship through the Royal Commission Yanbu Colleges and Institutes. Subject Editor J. A. Yeh. (*Corresponding author: Hongrui Jiang.*)

Y. D. Almoallem is with the Department of Electrical and Computer Engineering, University of Wisconsin–Madison, Madison, WI 53706 USA (e-mail: yalmoallem@wisc.edu).

H. Jiang is with the Department of Electrical and Computer Engineering, also with the Department of Biomedical Engineering, also with the Department of Materials Science and Engineering, also with the Department of Ophthalmology and Visual Sciences, and also with the McPherson Eye Research Institute, University of Wisconsin–Madison, Madison, WI 53706 USA (e-mail: hongrui@engr.wisc.edu).

Color versions of one or more of the figures in this paper are available online at <http://ieeexplore.ieee.org>.

Digital Object Identifier 10.1109/JMEMS.2017.2711966

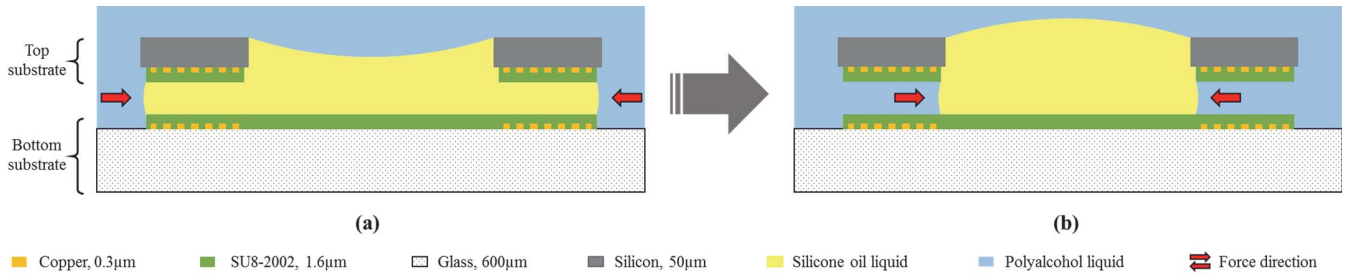


Fig. 1. Schematic of a cross-sectional view of the proposed device with DSD (not to scale). Both lens liquid (silicone oil) and ambient liquid (polyalcohol) are shown here. (a) A concave lens at the relaxed state without the DEP force. (b) A convex lens after liquid displacement with the DEP force applied via the electrodes in the capacitive chamber. The force is directed inward as indicated by red arrows.

force (\vec{F}) at the phase boundary between the two liquids, which results in a boundary displacement, as per the following equation [15]:

$$\vec{F} = -\frac{\epsilon_0}{2}\nabla[(\epsilon_1 - \epsilon_2)|\vec{E}|^2] \quad (1)$$

where ϵ_0 , ϵ_1 and ϵ_2 represent the permittivity of free space, ambient liquid (polar) and lens liquid (non-polar), respectively. $|\vec{E}|$ denotes the magnitude of the electric field across the interface between the two liquids.

The design of the device consists of two distinct sets of electrodes. Each electrode set is at a distinct layer on a different substrate. The spacing between the top and bottom electrodes results in a capacitive electrode structure, where the displacement of the liquid boundary occurs back and forth, causing lens curvature tuning. This space is referred to as the capacitive chamber. The lens liquid (here, silicone oil) is selected to have a lower dielectric constant ($\epsilon_2 < 10$) than the ambient liquid (here, polyalcohol, $\epsilon_1 \approx 80$), which directs the DEP force to squeeze the oil inside the aforementioned capacitive chamber inward, as indicated in Fig. 1. On the other hand, the refractive indices of silicone oil ($n_1 = 1.49$) is greater than polyalcohol solution ($n_2 = 1.39$). Therefore, the lens curves upward and the contact angle begins to increase from negative to positive based on the available oil volume in the capacitive chamber structure. Noticeably, the amount of oil determines the range of contact angle within which the device can operate, i.e. negative or positive range. In this work, a device of our capacitive electrode structure is named double-sided design (DSD), whereas a device with a single-sided (bottom) electrode design is named single-sided design (SSD), as in [15]–[17].

B. Miniature Lens Structure

The device structure is designed to reduce the level of the driving voltage. To that end, the following objectives need to be fulfilled: (I) increasing DEP force that displaces the phase boundary while tuning the lens focal length; as well as (II) reducing other opposing forces (e.g. surface friction) encountered during the tuning of the miniature lens curvature.

Increasing the stimulating force is achieved through sharpening the electric field gradient by doubling the spatial peak of the magnitude of the electric field. Since the spatial distance between the peaks of $|\vec{E}|$ is fixed by the electrode

spacing, the spatial gradient would vary proportionally to the peak in $|\vec{E}|$. Doubling $|\vec{E}|$ is attained by using the capacitive (double-sided structure) electrode, as shown in Fig. 1, instead of the single-sided bottom electrode used in SSD. The electric field between the capacitive plates is added constructively to increase the magnitude of the electric field. Equation (1) shows that the DEP force is proportional to the square of the $|\vec{E}|$ gradient. An alternative perspective is that in DSD devices, there are two driving forces in the capacitive chamber from both the top and the bottom, instead of from only the bottom in SSD devices.

One design aspect to consider is the liquid volume that needs to be displaced during focal length tuning. A comparison between SSD and DSD devices is shown in Fig. 2, where the amount of displaced liquid volume is highlighted (light-shading). These examples compare devices at two different, arbitrarily chosen starting contact angles: 20° and 60° . All have the same outer diameter of 2mm and inner diameter of 1mm. In DSD, the lens edge is pinned at a fixed, smaller radius (1mm), whereas in SSD, the lens edge is displaced from the outer radius (2mm) to inner radius (1mm). The liquid boundary is displaced over the green range, as shown in Fig. 2, which is incorporated in both designs to have similar hydrophobicity level. The displaced volumes for both designs are calculated using MATLAB and the details are presented in the next section along with optical power calculation. The results show that the DSD devices based on chamber size can offer smaller, similar, or bigger change in the optical power compared with SSD devices. However, the driving voltage to displace similar amount of liquids for similar focal tuning is much lower, as shown later.

A few factors are considered in the design to reduce the frictional resistance force. One factor is the pinning of the miniature lens edges at a fixed point located at the central opening of the top substrate. Another factor is by reducing the volume of the displaced liquid during the lens curvature adjustment process. The amount of work required to tune the lens is proportional to the volume of liquid that needs to be displaced. As shown in Fig. 2(a) and (d), the SSD lens cap encompasses the entire lens liquid, whereas the DSD lens cap represents a smaller portion of the lens liquid. In SSD, the displaced liquid volume is a function of the starting contact angle in such a way that the liquid volume increases as the starting contact angle increases. In comparison to the

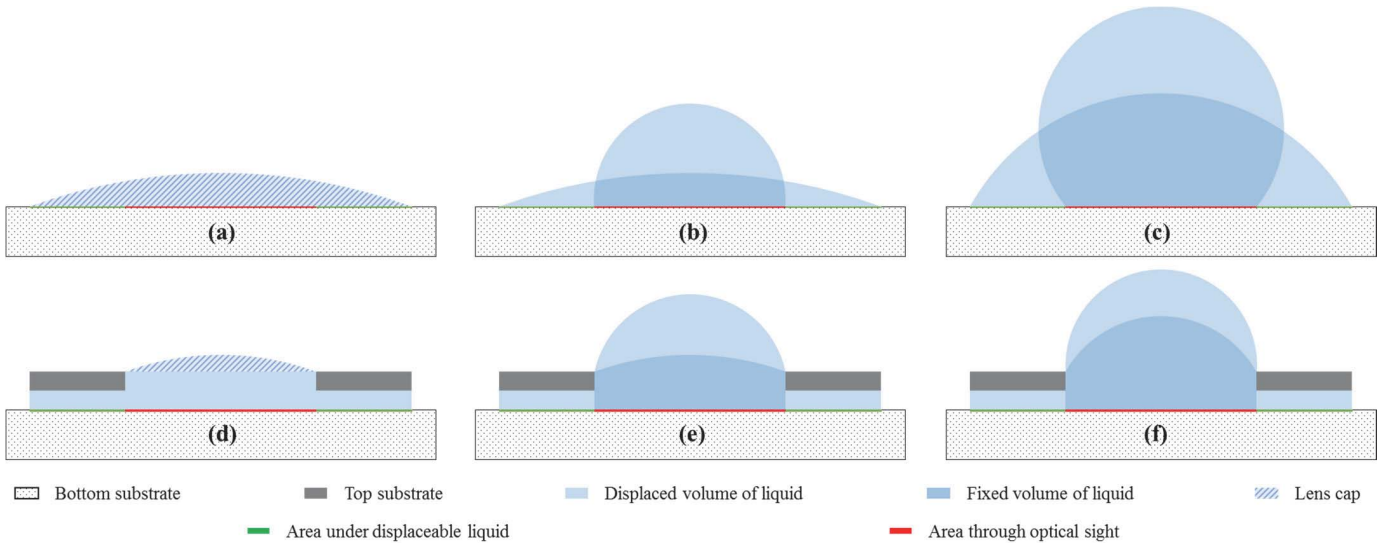


Fig. 2. Comparing cross-section view of Single-Sided Design (SSD) with Double-Sided Design (DSD). Only oil is shown without ambient liquid. The droplet is squeezed from the starting state (relaxed) covering red and green ranges (2mm diameter) to the final state (under DEP force) covering only the red range (1 mm diameter). (a) Initial contact angle of the SSD lens cap is 20°. (b) SSD 1st example: contact angle varies from 20° till 93°. (c) SSD 2nd example: contact angle varies from 60° till 129°. (d) DSD lens cap initial contact angle is 20° and chamber height is 50 μm . (e) DSD 1st example: contact angle varies from 20° till 78°, (f) DSD 2nd example: contact angle varies from 60° till 93°.

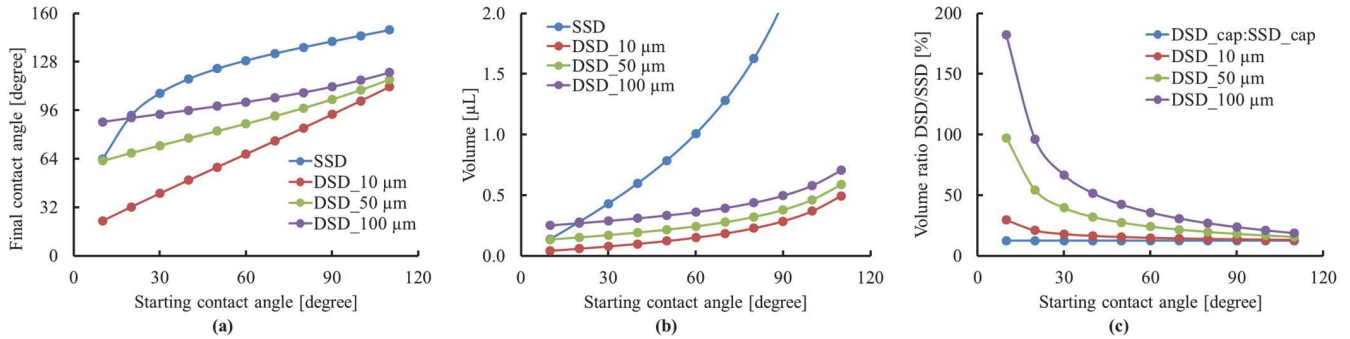


Fig. 3. Analyzing the lens volume based on the starting contact angle for a device of 2mm outer diameter and 1mm inner diameter. (a) The relation between starting and ending contact angles for SSD and DSD with three different chamber heights. (b) Volume of lens based on the starting contact angle for SSD and DSD with three different chamber heights. (c) The ratio of lens volume of DSD to that of SSD with three different chamber heights and the ratio of the cap volume of DSD to that of SSD.

DSD structure, there is a fixed displaced volume exactly equal to the capacitive chamber volume. This gives us an idea about the amount of work needed for each device irrespective of the liquid volume or starting contact angle. For the examples given in Fig. 2, the top row shows the first SSD example with a contact angle from 20° to 93°, with its cap volume being 280 nL, whereas the first DSD example shown in the bottom row has a contact angle from 20° to 78°, with its cap volume being merely 35 nL.

In SSD, both radial (toward the miniature lens central axis) and vertical (normal to substrate surface) force components exist. In comparison, the DSD structure only has the radial component and the vertical component is eliminated. Therefore, the problem is reduced to a 1D problem with the radial force. In the macroscale, DSD structure cancels the vertical component of DEP force and keep the horizontal radial component of DEP force pressurizing fluidic inward rather than changing the contact angle.

Fig. 3(a) shows the behavior of the starting and ending contact angles with different liquid volumes. The ratio between

the volume of the lens cap of the DSD and SSD is kept constant at all starting contact angles as shown in Fig. 3(c) and this constant relationship is explained mathematically as follows. For a given contact angle, the DSD cap volume is equal to only 12.5% of the SSD cap volume. This result is due to the fact that the lens radius is forced to shrink to half. The contact angles are equal to $\theta_{\text{SSD}} = \theta_{\text{DSD}} = \theta$, and the base radius of the cap in SSD doubles that in the DSD, i.e. $r_{\text{SSD}} = 2 \cdot r_{\text{DSD}}$. The spherical cap volume (V) as a function of the radius of curvature (R) and the contact angle (θ) is given by following equation:

$$V = \int_x^R \pi (R^2 - x^2) dx = \frac{\pi}{3} R^3 (\cos \theta + 2) (\cos \theta - 1)^2 \quad (2)$$

Using trigonometric equations with the relation, $R = \frac{r}{\cos \theta}$, the relation between the DSD and SSD volumes is calculated to be:

$$\frac{V_{\text{DSD}}}{V_{\text{SSD}}} = \left(\frac{R_{\text{DSD}}}{R_{\text{SSD}}} \right)^3 = 12.5\% \quad (3)$$

TABLE I
SSD AND DSD VOLUME AND OPTICAL CALCULATION

SSD								
Lens #	R_S [mm]	CA_S [°]	H_F [mm]	R_F [mm]	CA_F [°]	F_S [mm]	F_F [mm]	V_{DISP} [nL]
[1]	4.227	14	0.398	0.513	77	39.282	2.767	111
[2]	3.113	19	0.500	0.500	90	28.706	2.494	150
DSD								
Lens #	R_S [mm]	CA_S [°]	H_F [mm]	R_F [mm]	CA_F [°]	F_S [mm]	F_F [mm]	V_{DISP} [nL]
[1]	4.227	7	0.295	0.571	61	39.275	3.573	118
[2]	3.113	9	0.303	0.564	62	28.722	3.477	118

For each design two examples are given.

In other words, the DSD cap volume is about one eighth of the SSD cap volume regardless of the chamber volume, as shown in Fig. 3(c), the line labeled in a legend as DSD_cap: SSD_cap.

The lens cap volume has been decreased in the DSD, keeping the same contact angle as used in the SSD, as shown with the dark-blue lined-diagonal in Fig. 2 (a) and (b). In SSD, the lens needs to cover the optical area in the center (red) as well as the electrode active area (green). However, in DSD, the lens only needs to cover the optical area in the center (red) while it is pinned at the edge. The capacitive chamber supplies the additional volume needed for tuning the focal length. The electrode active region where forces are applied is separated from the area at which the contact angle is formed. The liquid lens edges are pinned at the top substrate opening of the fixed structure where no friction force is encountered. The forces are applied at the active region of the electrode where the contact angle of the liquids are maintained constant but only moving back and forth against low resistance hydrophobic surfaces between the top and bottom structures.

C. Electric Field Simulation

Electromagnetic simulations were employed to estimate the increase in the $|\vec{E}|$ gradient in the proposed DSD device. Ansys-Maxwell software was used to simulate both the SSD and DSD electrode structures. Electrostatic solution was considered and applied voltage was kept at 100V. The electrode spacing was kept the same at $35\mu\text{m}$. The capacitive chamber height used in DSD was $50\mu\text{m}$. In isometric view as shown in Fig. 4(a) and (c), the particle density was intentionally kept low to visualize the electrode underneath. The particle density was increased in the 2D side view plot to test $|\vec{E}|$ gradient patterns accurately, as shown in Fig. 4(b) and (d). Clipping tools was used to view the internal $|\vec{E}|$ gradient patterns in 2D.

To assess the $|\vec{E}|$ gradient, an example was given by measuring $|\vec{E}|$ along a 50° tilted line as shown in Fig. 4(e). The DSD shows a sharper increase per distance, $0.1 - 6 \text{ V}/\mu\text{m}$ in a $30\mu\text{m}$ distance compared with SSD, in which the increase is $0.6 - 4 \text{ V}/\mu\text{m}$ in a $39\mu\text{m}$ distance. Therefore, total $\nabla|\vec{E}|/\nabla D$ is more than doubled from SSD to DSD, where D is the distance. Observing an individual step slope gives a closer picture of the $|\vec{E}|$ gradient. The ratio between DSD and SSD of the maximum value of $\nabla|\vec{E}|/\nabla D$ steps can reach $3\times$. This indicates a potential increase in the DEP force by a factor of 9 as per equation (1). Fig. 4(f) shows the electrical field direction

in DSD, simulated in Ansys Maxwell. The DSD lens is not sensitive to shifting between the top and bottom substrates. Simulation results show that the change in the total $\nabla|\vec{E}|/\nabla D$ is less than 5% when different displacements is introduced: $5\mu\text{m}$ shift, $10\mu\text{m}$ shift and $50\mu\text{m}$ shift. Distribution of the electric field does not experience any significant variation either.

D. Optical Simulation

The optical power defines the strength of the lens to converge light in the case of convex lens. The liquid volume initially dispensed defines the range of optical power through which a given miniature lens can be tuned. In Fig. 2, the optical focal length range differs based on the initial contact angle, which is a function of the dispensed liquid volume. In this section, the starting radius of curvature (R_S) rather than starting contact angle (CA_S) is kept the same for both SSD and DSD for comparison. MATLAB was used to calculate the spatial dimensions of a miniature lens. Table I shows two examples to compare between the SSD and DSD. Each example calculates the dimensions of the lens cap at the starting state (relaxed) and the final state (under DEP force). R_S is selected to have a realistic initial contact angle ($>10^\circ$) and proper final contact angle ($\leq 90^\circ$).

The final cap height (H_F) and radius of curvature (R_F) are presented in the table to ensure that the lens is not over-tuned, passing the inner radius of electrode (0.500 mm). The table continues to show the other variables, namely final contact angle (CA_F) starting and final back focal length (F_S & F_F) and displaced volume (V_{DISP}). MATLAB was employed to calculate V_{DISP} for DSD, which is simply equal to the capacitive chamber volume. For the SSD, the MATLAB code first defined the integration boundary by finding the intersecting point between the two curves defining the lens profile in the starting and final states. Then, the code took the integral to find the volume enclosed by these two surfaces. R_S was varied and all the parameters were recalculated for both the SSD and the DSD, (see Fig. 5 for V_{DISP} vs. R_S). SSD V_{DISP} is more than DSD V_{DISP} when R_S is below about 4 mm. The miniature lens focal length calculation can be categorized under the thick lens class where the thin lens approximation is no longer valid. To calculate the lens optical power, we used ZEMAX software to more accurately simulate the lens and find the back focal lengths (Table I). Focal lengths were found at the smallest spot size using a single wavelength ($\lambda = 486 \text{ nm}$) (see Fig. 6). Table I shows that V_{DISP} in DSD is constant

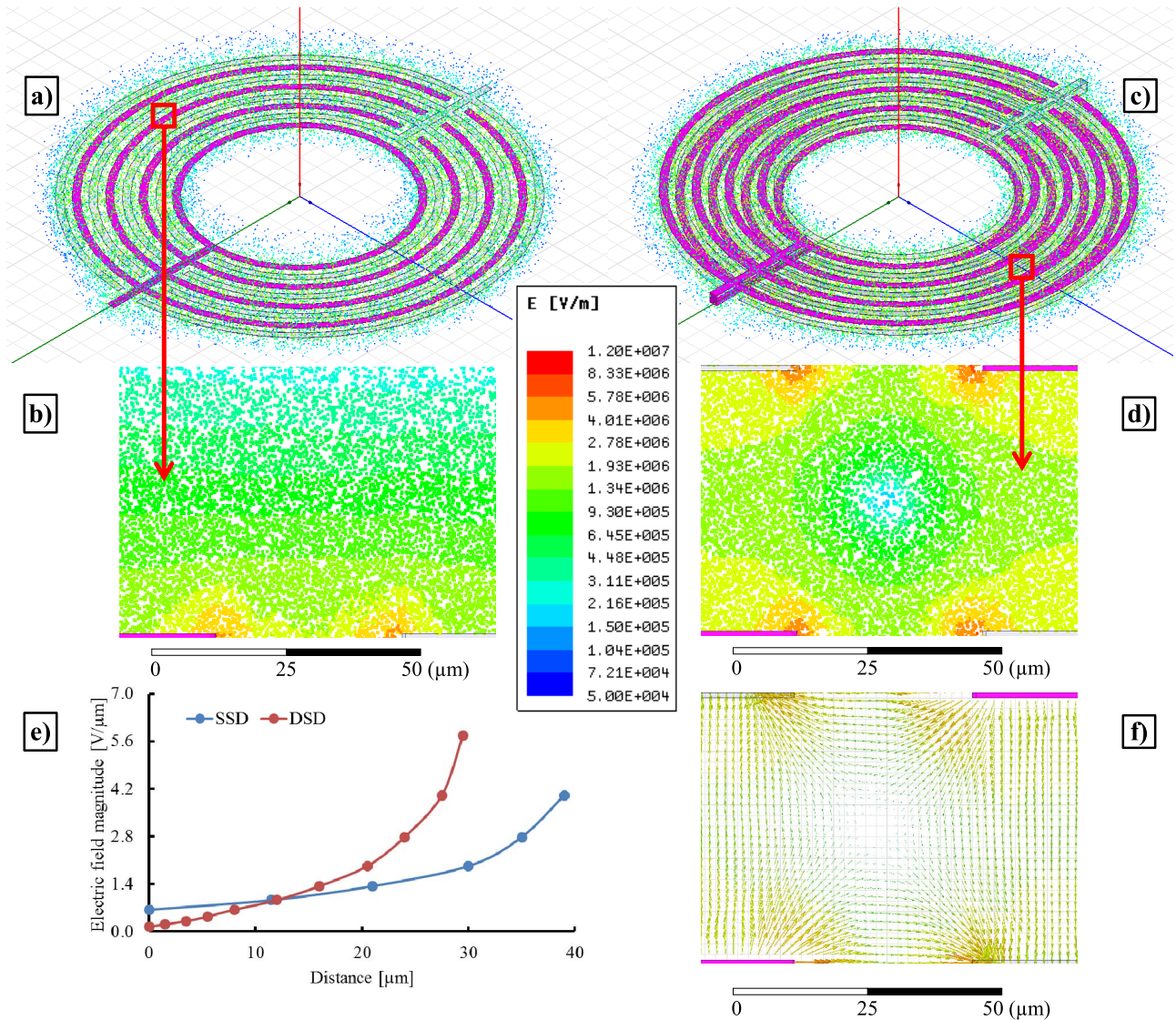


Fig. 4. Finite element simulation of the electric field comparing SSD (left) and DSD (right) using Ansys Maxwell. (a) 3D isometric view shows the entire electrode of SSD including electric field scale. (b) 2D close-up view of SSD shows gradient of electric field. (c) 3D isometric shows the entire electrodes of DSD. (d) 2D close-up view of DSD shows gradient of electric field. (e) Change of $|\vec{E}|$ as a function of distance. DSD shows sharper increase for the same distance, from 0.1 to 6 V/μm compared with from 0.5 to 4 V/μm in the case of SSD. (f) The electrical field direction in DSD.

for both examples while the $F_S - F_F$ range is comparable with that in SSD in which V_{DISP} varies. Therefore, the work needed to operate DSD is constant regardless of CA_S . The inner electrode limits the aperture of both DSD and SSD; hence, their effective apertures are similar.

E. Electrode Design

Multiple electrode designs were tested with the DSD structure. Both top and bottom electrodes were kept similar. Circular and radially-interdigitated electrodes were used. The gap between the interdigitated electrodes was varied from 35 μm all the way to 7 μm. Further electrode inter-branching was introduced to generate additional non-uniformity in the fringing electric field.

F. Device Fabrication

The DSD device consists of two substrates, top and bottom, which were fabricated separately and then assembled together.

The SSD device consists of just the bottom substrate. The bottom substrate fabrication process is shown in Fig. 7(a)-(c) and the top substrate fabrication process is shown in Fig. 7(d)-(g).

The bottom substrate was fabricated on a fused silica glass wafer cleaned in a Piranha solution. After a 300-nm-thick copper layer was deposited in a metal evaporator, the electrode was patterned by standard photolithography processes, using S1813 photoresist (PR) to protect the electrode during a subsequent wet etching step using a copper etchant, as shown in Fig. 7(a). Then, a 1.6-μm-thick SU-8 2002 PR (MicroChem Corp., 200 Flanders Road Westborough, MA 01581, USA) dielectric layer was spin-coated and patterned in order to insulate the electrode layer, as shown in Fig. 7(b). The adhesion of SU-8 to glass was improved by ramped baking and ensuring wafer surface cleanliness. The thickness of this layer fundamentally affects the DEP force magnitude. The dielectric layer here was designed

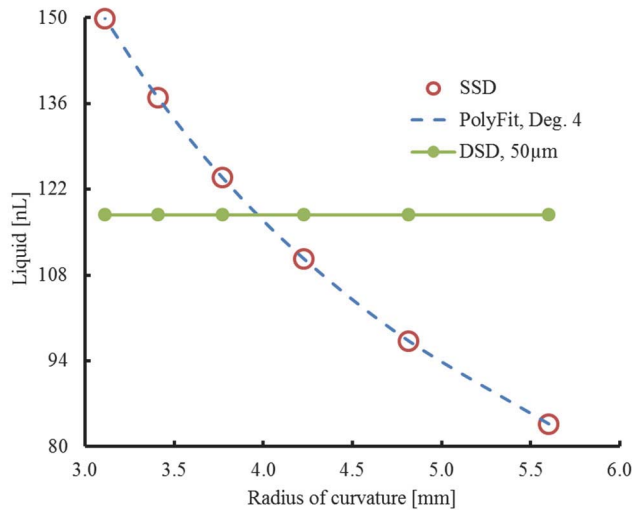


Fig. 5. Comparison between SSD and DSD in terms of the displaced volume required for lens tuning as a function of R_S . DSD V_{DISP} is constant since the chamber volume is fixed, whereas SSD V_{DISP} decreases as R_S increases.

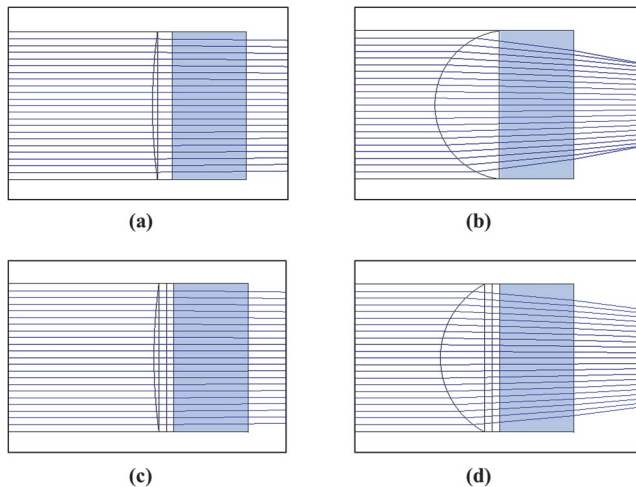


Fig. 6. Diagrams of the ZEMAX simulations of the lens to calculate its optical power. On the left shows the relaxed state and on the right shows the lens under the DEP force. (a)-(b) In SSD, one layer of lens liquid is used on the glass slides (blue-shaded). (c)-(d) In DSD, additional layers are added to represent the chamber height.

to cover the central part of the lens, which made oil droplet placement easier during the final assembly phase.

The last layer of the bottom substrate (shown in Fig. 7(c)) was a 48- μm -thick spacer layer attained by spin-coating and patterning an SU-8 50 PR (MicroChem Corp., 200 Flanders Road Westborough, MA 01581, USA). Both SU-8 layers were hard baked. Similar to SU-8 2002, the adhesion of SU-8 50 to glass was improved by ramped baking. As the final step for the bottom substrate, a surface treatment was performed inside a plasma chamber with sulfur hexafluoride (SF_6) to make the SU-8 surface more hydrophobic [12].

The top substrate had an additional fabrication complexity of creating a hole all the way through the complete thickness of the wafer after processing all layers. In this work, the top substrate was fabricated on a thin Si wafer, which enabled etching through the complete thickness easier. The thin Si wafer was chosen to be a 50- μm -thick wafer.

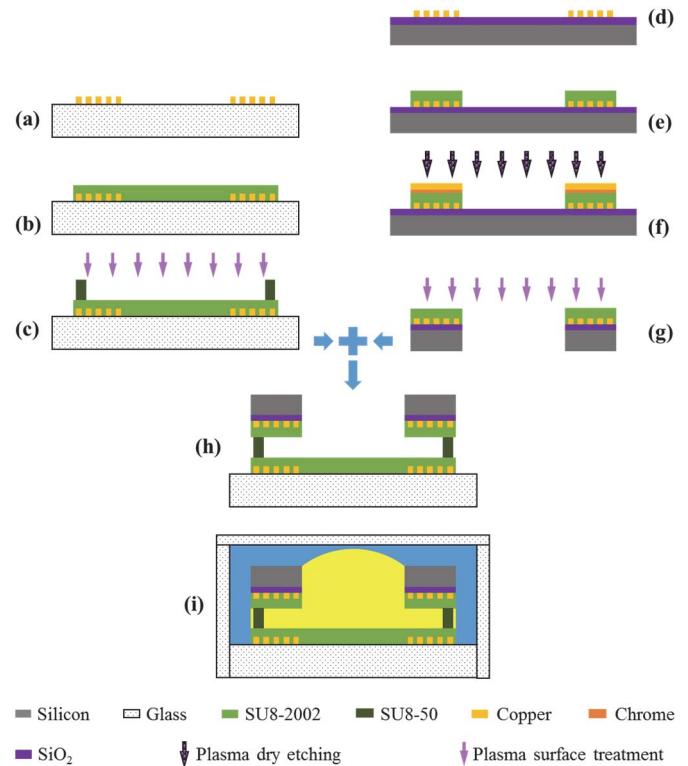


Fig. 7. Fabrication process flow. The bottom substrate is shown in (a)-(c) and the top substrate is shown in (d)-(g). The assembly is shown in (h)-(i). (a) Depositing/patterning the copper electrode layer on a glass wafer for the bottom substrate. (b) Spin-coating/patterning SU-8 2002 dielectric layer for the bottom substrate. (c) Spin-coating/patterning SU-8 50 spacer layer and surface treatment. (d) Top substrate fabrication on a thin Si wafer with deposited dioxide layer and depositing/patterning the copper electrode layer. (e) Spin-coating/patterning SU-8 2002 dielectric layer for the top substrate. (f) Depositing/patterning the chromium-copper dry-etching mask and dry-etching Si in a plasma. (g) Removing the dry-etching mask and surface treatment. (h) Assembling top and bottom substrates with alignment under a microscope. (i) Chamber construction and liquid filling.

After cleaning the thin Si wafer in a Piranha solution, a 200-nm-thick of silicon dioxide (SiO_2) layer was deposited in a dielectric evaporator as the insulating layer in order to avoid current leakage between electrodes through the underlying Si substrate. Then, similar to the bottom substrate, a 300-nm-thick copper electrode layer was deposited, patterned by S1813 PR, and wet etched, as shown in Fig. 7(d). Subsequently, a 1.6- μm -thick SU-8 2002 PR dielectric layer was spin-coated and patterned, as shown in Fig. 7(e). SU-8 baking step during the photolithography patterning was done with a ramped function to increase the adhesion to the underlying SiO_2 layer. For the SU-8 2002 layer, the hard baking step was essential to ensure all solvent evaporation before Si plasma dry-etching.

Fig. 7(f) shows the Si dry-etching step, where the wafer was prepared for etching by depositing a copper hard mask layer. First, a thin layer (5 nm) of chromium and then a 500-nm-thick copper hard mask layer were deposited using a metal evaporator. The chromium layer was employed to improve the adhesion of copper onto SU-8 and additionally to make the dry-etching process more stable, preventing mask cracking due to mechanical and thermal stresses. This copper

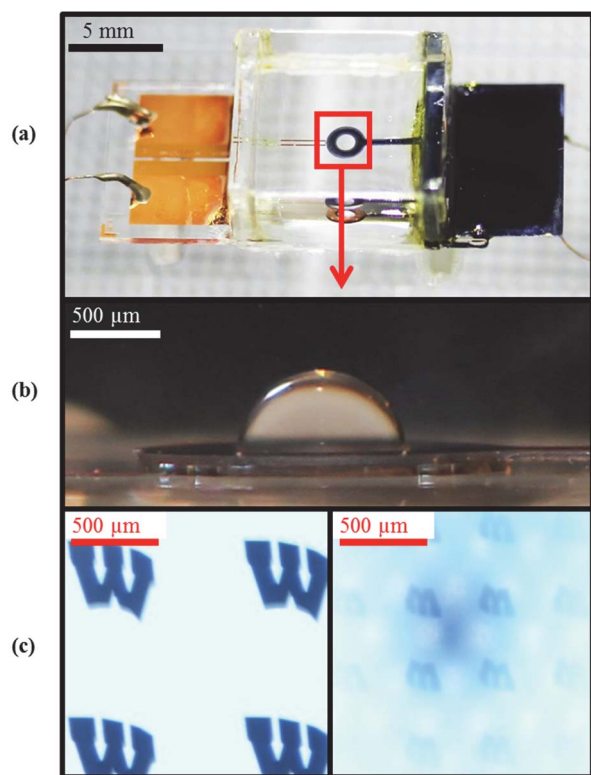


Fig. 8. (a) Device picture after the assembly with liquids. (b) Close-up side-view of the liquid miniature lens. (c) Pictures taken under a microscope. Left: focused at the object plane; right: focused at the image plane.

hard mask was patterned through a similar photolithography step used for patterning the electrodes. However, soft baking was done here inside an oven instead of using a hot plate in the case of the electrode patterning. The oven was used to avoid cracks in the copper dry-etching mask. Similar to the electrode patterning, the mask was patterned in diluted APS-100 copper etchant. After the wafer was placed in a vacuum chamber below 0.133 Pa (1 mTorr) for about 60 minutes to help evaporate any left-over solvent content, the plasma Si dry-etching process was started. The Si was etched using a plasma with SF₆ gas in a PlasmaTherm 790 ICP/RIE Etcher. The parameters were 30 SCCM (standard cubic centimeters per minute) of SF₆, and 30 SCCM of O₂. The pressure was 2.67 Pa (20 mTorr). The RIE power was 50 W and the ICP power 400 W. The dry-etching process took about 120 minutes.

After the plasma etching process was finished, the individual devices were once again placed in a diluted copper etchant solution to remove the copper hard mask layers. The individual devices were etched, rinsed and dried on a hot plate with care to avoid cracking. The last fabrication step was the same as for the bottom substrate, where a surface treatment was performed inside plasma chamber, as shown in Fig. 7(g). The backside of the thin wafer was kept clean during the fabrication steps.

Another issue related to the thin wafer handling was bonding and un-bonding from carrier wafer. Here the device was fabricated without a carrier wafer for the following reasons. Usage of bonding material is critical since it should be resistant to all chemical used throughout the fabrication process.

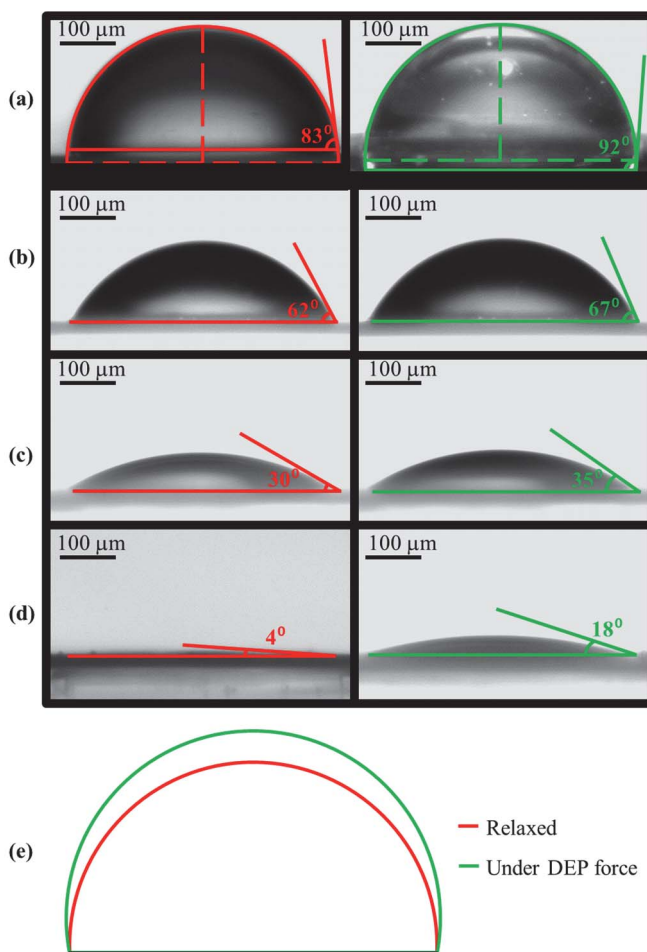


Fig. 9. Pictures of the miniature lens surface curvatures obtained via a goniometer. They show the contact angle for different oil volumes where the left column demonstrates the lens at its relaxed state without DEP force, and the right column the lens under a DEP force. (a) Volume is 370 nL. (b) Volume is 270 nL. (c) Volume is 240 nL. (d) Volume is 160 nL. (e) A schematic comparing the goniometer pictures in (a) with both curvatures in the same plot. The red line shows the relaxed state (0 V) and the green line shows the state under a DEP force (22 V) where the height increases from 456 to 542 μm .

Creating any bubbles during intermediate fabrication steps can cause wafer breakage during any subsequent low-pressure step.

Device assembly is shown in Fig. 7(h)-(i). The top substrate was placed faced down on the bottom substrate and epoxied to the spacer pad under a microscope for precise positioning, as shown in Fig. 7(h). Glass chamber walls were fixed to the sides in such a way that the sight is clear under a goniometer for imaging the side-view of the lens droplet and hence contact angle measurements, as shown in Fig. 7(i). Finally, silicone oil (Dow Corning 550, Dow Corning Corp., Midland, MI, USA) was dispensed at the central hole and the ambient medium was filled with polyalcohol solution. A glass cap was used to seal the chamber.

Silicone oil was used to wet the central region of the lens and then polyalcohol was used to fill the chamber as the ambient medium. Later, silicone oil volume was increased or decreased to control the initial lens contact angle under the goniometer view with the help of a stationary sharp syringe connected to a flexible extension tube. Fig. 8 shows

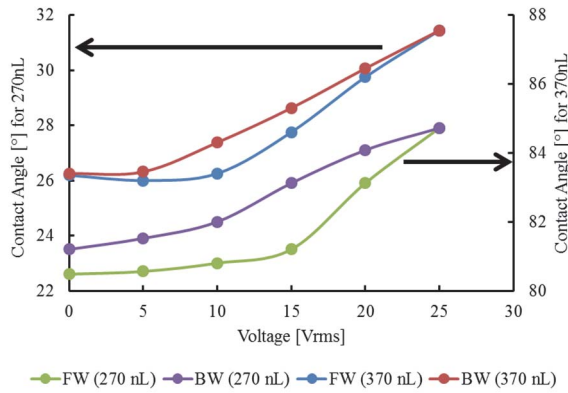


Fig. 10. Measured contact angle as a function of the applied voltage. It shows the device hysteresis for two different lenses with different oil volumes. Left axis: oil volume is 270 nL; right axis: oil volume is 370 nL.

the device after the assembly with liquids. The miniature lens cap was captured from the side as shown in Fig. 8(b). The miniature lens inverted the object (letter W) at the image plane as shown in Fig. 8(c).

III. RESULTS AND DISCUSSION

The fabricated tunable miniature lens was characterized through the following methods: the contact angle measurement, ZEMAX simulation, measurement utilizing the 1951-USAF resolution test chart, and a Shack-Hartmann wavefront sensor.

The contact angle was measured using a goniometer tool (OCA 15+, DataPhysics Instruments Inc., Filderstadt, Germany). The chamber was designed with flat glass walls to allow a clear side-view of the miniature lens. Epoxy was applied to fix those sidewalls in position without blocking side-view of the lens.

The shape of the miniature lens was captured while bulging out of the top substrate opening, as shown in Fig. 9. An excitation square-wave voltage was applied across the electrodes (for both the top and bottom substrates) at 10 kHz, and the measured RMS voltage level was within the range from zero to 25 V. The droplet was enlarged by squeezing the chamber oil into the top substrate opening. As seen in Fig. 9(a), the droplet contact angle was observed to change from 83° at zero V to 92° at 22 V. Measured contact angles were subsequently used to calculate the lens profile as discussed previously. Using ZEMAX, the miniature lens was simulated to calculate the back focal length, which was found to vary from 2.528 mm to 2.421 mm, as shown in Table II. This change in focal length was relatively small because the radius of curvature of the lens decreased from 503.8 to 500.0 μm at a contact angle equal to 90° and then increased back to 500.3 μm afterward. Therefore, the net focal length change was small in this example. The miniature lens was then tested at different volumes of lens oil as shown in Fig. 9(a)-(d), varying between 160 and 370 nL. Accordingly, the starting contact angle varied from 4° to 83° , and the final contact angle was observed to change from 18° to 92° . Therefore, we tested the lens with different volumes that gave the calculated back focal length range from 2.421 mm to 67.051 mm.

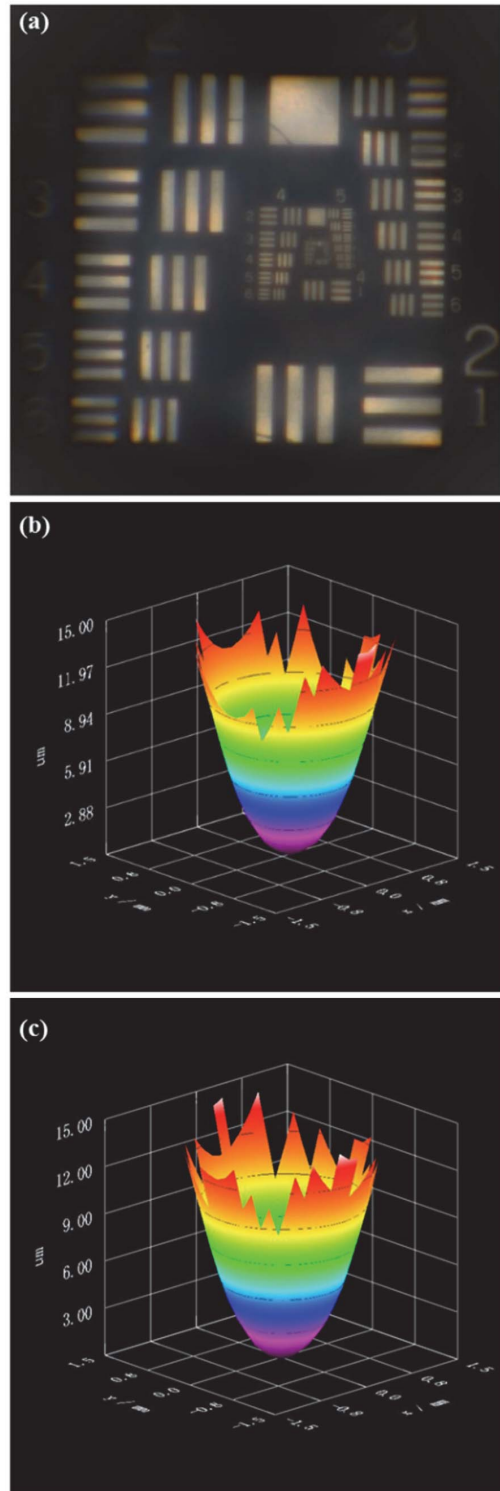


Fig. 11. Optical characterization of the miniature lens. (a) Image of a 1951-USAF resolution test chart. The miniature lens is capable of resolving group 5, element 3. (b) Miniature lens surface profile obtained using a Shack-Hartmann setup, with the oil volume of 370 nL. The applied voltage is 0 V. (c) Similar to (b), only that the applied voltage is 25 V.

Fig. 10 shows the effect of hysteresis on the contact angle by applying increasing and decreasing voltages using the same power supply with a 10 kHz square wave from zero to 25 V. Two examples are shown with different volumes: 370 nL and 270 nL. The hysteresis shown is comparable to those reported

TABLE II
DSD FOCAL LENGTH CALCULATION

Lens #	CA _s [°]	At 0 V (10 kHz square wave form)			At 25 V (10 kHz square wave form)			
		R _s [mm]	H _s [mm]	F _s [mm]	CA _F [°]	R _F [mm]	H _F [mm]	F _F [mm]
[1]	83	0.5038	0.4924	2.528	92	0.5003	0.5678	2.421
[2]	62	0.5663	0.3504	3.509	76	0.5153	0.4406	2.741
[3]	30	1.0000	0.1840	8.341	35	0.8717	0.2076	7.017
[4]	4	7.1678	0.0675	67.051	18	1.6180	0.1292	14.438

Left half shows the lens at its relaxed state (0 V). Right half shows the lens under a DEP force (25 V). Four examples are given.

previously, and is typical of electrohydrodynamically actuated liquid miniature lenses.

A measurement setup was prepared using a microscope to characterize the resolution of our miniature lens. A 1951-USAF test chart was placed behind the miniature lens at the relaxed state (0 V) and the microscope captured the image, as shown in Fig. 11(a). The miniature lens was capable of resolving group 5, element 3, corresponding to a resolution of 40.3 lp / mm. In Fig. 8(c), the microscope pictures were obtained using 4× magnification lens. They represent object-image pairs where the microscope was focused to capture pictures at relative planes: object (left-side) and image (right-side) planes. Image inversion and magnification are clearly noticeable compared with the originally captured picture of the object.

The miniature lens profile was measured using a setup that encompassed a Shack-Hartmann wavefront sensor as described in [28]. The setup was modified to fit the miniature lens aperture of 1 mm. Results are shown in Fig. 11(b)-(c). The miniature lens profile was measured at the relaxed state as well as under a DEP force.

The DSD results show the potential of driving the miniature lens electrically with voltages ranging from zero to 25 V. As presented in the introduction, other SSD lenses require driving voltages at much higher level. The much lowered driving voltage is a prominent advantage of our DSD electrodes.

IV. CONCLUSION

Tunable liquid miniature lenses with a double-sided design of electrode structures were fabricated and tuned at a much lower level of voltage, as compared with more conventional single-sided designs of the actuation electrodes. The electromagnetic simulation results showed good matching with experimental measurements. Both demonstrated increase in the DEP force which in turn allowed for the focal tuning of the miniature lens at a much lower voltage level of 25 V compared with 100+ V in more traditional designs. The tested miniature lens showed a good resolution power. The measured contact angle range was used to find the tunable focal length range. This design enabled us to drive a tunable miniature lenses at lower voltage levels based on dielectrophoretic designs. In future efforts, we aim to further reduce surface friction forces to improve focal range and expand fabrication from single devices to a lens array.

ACKNOWLEDGMENT

The authors would like to thank Professor James P. Blanchard for access to the electromagnetic simulation software (Ansys-Maxwell). This research utilized NSF supported shared facilities at the University of Wisconsin. They are grateful to Dr. A. O. Ashtiani, K. Van Grinsven, and J. Fernandes for technical assistance and discussion. They would like to thank also the staff at the Wisconsin Center for Applied Microelectronics (WCAM) at the University of Wisconsin-Madison for technical support and consultation in fabrication process.

REFERENCES

- [1] L. Dong, A. K. Agarwal, D. J. Beebe, and H. Jiang, "Adaptive liquid microlenses activated by stimuli-responsive hydrogels," *Nature*, vol. 442, no. 7102, pp. 551–554, 2006.
- [2] P.-G. de Gennes, F. Brochard-Wyart, and D. Quere, *Capillarity and Wetting Phenomena: Drops, Bubbles, Pearls, Waves*. New York, NY, USA: Springer, 2013.
- [3] J. S. Rowlinson and B. Widom, *Molecular Theory of Capillarity*. North Chelmsford, MA, USA: Courier Corporation, 2013.
- [4] J. N. Israelachvili, *Intermolecular and Surface Forces*, 3rd ed. New York, NY, USA: Academic, 2011.
- [5] H. Ren, D. W. Fox, B. Wu, and S. T. Wu, "Liquid crystal lens with large focal length tunability and low operating voltage," *Opt. Exp.*, vol. 15, no. 18, pp. 11328–11335, 2007.
- [6] J. Kim, J. Kim, J. H. Na, B. Lee, and S. D. Lee, "Liquid crystal-based square lens array with tunable focal length," *Opt. Exp.*, vol. 22, no. 3, pp. 3316–3324, 2014.
- [7] L. Li, Q.-H. Wang, and W. Jiang, "Liquid lens with double tunable surfaces for large power tunability and improved optical performance," *J. Opt.*, vol. 13, no. 11, 2011, Art. no. 115503.
- [8] A. O. Ashtiani and H. Jiang, "Tunable microlens actuated via a thermoelectrically driven liquid heat engine," *J. Appl. Phys.*, vol. 115, no. 24, p. 243103, 2014.
- [9] L. Dong and H. Jiang, "pH-adaptive microlenses using pinned liquid-liquid interfaces actuated by pH-responsive hydrogel," *Appl. Phys. Lett.*, vol. 89, no. 21, p. 211120, 2006.
- [10] W. Xiao and S. Hardt, "An adaptive liquid microlens driven by a ferrofluidic transducer," *J. Micromech. Microeng.*, vol. 20, no. 5, p. 055032, 2010.
- [11] C. A. López and A. H. Hirsra, "Fast focusing using a pinned-contact oscillating liquid lens," *Nature Photon.*, vol. 2, no. 10, pp. 610–613, 2008.
- [12] A. O. Ashtiani and H. Jiang, "Design and fabrication of an electrohydrodynamically actuated microlens with areal density modulated electrodes," *J. Micromech. Microeng.*, vol. 26, no. 1, p. 15004, 2016.
- [13] A. O. Ashtiani and H. Jiang, "An electrohydrodynamically actuated liquid microlens with areal density modulated electrodes," in *Proc. 18th Int. Conf. Solid-State Sens., Actuators, Microsyst. (TRANSDUCERS)*, Jun. 2015, pp. 2089–2092.
- [14] B. Berge and J. Pesieux, "Variable focal lens controlled by an external voltage: An application of electrowetting," *Eur. Phys. J. E*, vol. 3, no. 2, pp. 159–163, 2000.

- [15] Y.-S. Lu, H. Tu, Y. Xu, and H. Jiang, "Tunable dielectric liquid lens on flexible substrate," *Appl. Phys. Lett.*, vol. 103, no. 26, p. 261113, 2013.
- [16] H. Ren, H. Xianyu, S. Xu, and S. T. Wu, "Adaptive dielectric liquid lens," *Opt. Exp.*, vol. 16, no. 19, pp. 14954–14960, 2008.
- [17] C. C. Cheng, C. A. Chang, and J. A. Yeh, "Variable focus dielectric liquid droplet lens," *Opt. Exp.*, vol. 14, no. 9, pp. 4101–4106, 2006.
- [18] C. Li and H. Jiang, "Electrowetting-driven variable-focus microlens on flexible surfaces," *Appl. Phys. Lett.*, vol. 100, no. 23, p. 231105, 2012.
- [19] C. Li and H. Jiang, "Fabrication and characterization of flexible electrowetting on dielectrics (EWOD) microlens," *Micromachines*, vol. 5, no. 3, pp. 432–441, 2014.
- [20] T. Krupenkin, S. Yang, and P. Mach, "Tunable liquid microlens," *Appl. Phys. Lett.*, vol. 82, no. 3, pp. 316–318, 2003.
- [21] G. McHale, C. V. Brown, M. I. Newton, G. G. Wells, and N. Sampara, "Dielectrowetting driven spreading of droplets," *Phys. Rev. Lett.*, vol. 107, no. 18, p. 186101, 2011.
- [22] M. Xu, D. Xu, H. Ren, I.-S. Yoo, and Q.-H. Wang, "An adaptive liquid lens with radial interdigitated electrode," *J. Opt.*, vol. 16, no. 10, p. 105601, 2014.
- [23] C. G. Tsai, C.-N. Chen, L.-S. Cheng, C.-C. Cheng, J.-T. Yang, and J. A. Yeh, "Planar liquid confinement for optical centering of dielectric liquid lenses," *IEEE Photon. Technol. Lett.*, vol. 21, no. 19, pp. 1396–1398, Oct. 1, 2009.
- [24] C.-C. Yang, C. G. Tsai, and J. A. Yeh, "Miniaturization of dielectric liquid microlens in package," *Biomicrofluidics*, vol. 4, no. 4, p. 043006, 2010.
- [25] B. Jin, M. Xu, H. Ren, and Q.-H. Wang, "An adaptive liquid lens with a reciprocating movement in a cylindrical hole," *Opt. Exp.*, vol. 22, no. 25, pp. 31041–31049, 2014.
- [26] S. Xu, Y.-J. Lin, and S.-T. Wu, "Dielectric liquid microlens with well-shaped electrode," *Opt. Exp.*, vol. 17, no. 13, pp. 10499–10505, 2009.
- [27] M. Xu, X. Wang, and H. Ren, "Tunable focus liquid lens with radial-patterned electrode," *Micromachines*, vol. 6, no. 8, pp. 1157–1165, 2015.
- [28] C. Li, G. Hall, D. Zhu, H. Li, K. W. Eliceiri, and H. Jiang, "Three-dimensional surface profile measurement of microlenses using the Shack–Hartmann wavefront sensor," *J. Microelectromech. Syst.*, 21, no. 3, pp. 530–540, Jun. 2012.



Yousuf D. Almoallem received the B.S. and M.S. degrees in electrical engineering from the King Fahd University of Petroleum and Minerals, Dhahran, Saudi Arabia, in 2004 and 2011, respectively. He is currently pursuing the Ph.D. degree with the Department of Electrical and Computer Engineering, University of Wisconsin–Madison, Madison, WI, USA. Fellow is under sponsorship of the Saudi Government of Yanbu Royal Commission. His research interests include optical MEMS, tunable microlens, and low-voltage excitation.



Hongrui Jiang (S'98–M'02–SM'10–F'17) received the B.S. degree in physics from Peking University, Beijing, China, and the M.S. and Ph.D. degrees in electrical engineering from Cornell University, Ithaca, NY, USA, in 1999 and 2001, respectively. From 2001 to 2002, he was a Post-Doctoral Researcher at the Berkeley Sensor and Actuator Center, University of California at Berkeley. He is currently the Vilas Distinguished Achievement Professor and the Lynn H. Matthias Professor in engineering with the Department of Electrical and Computer Engineering, and a Faculty Affiliate with the Department of Biomedical Engineering, the Department of Materials Science and Engineering, and the Department of Ophthalmology and Visual Sciences, and a member of the McPherson Eye Research Institute, University of Wisconsin–Madison. His research interests are in microfabrication technology, biological and chemical microsensors, microactuators, optical microelectromechanical systems, smart materials and micro-/nanostructures, lab-on-chip, and biomimetics, and bioinspiration. He is a Member of the Editorial Board of the IEEE/ASME JOURNAL OF MICROELECTROMECHANICAL SYSTEMS.

Dr. Jiang is a fellow of the Institute of Physics, the Royal Society of Chemistry, and the American Institute for Medical and Biological Engineering. He was a recipient of the National Science Foundation CAREER Award and the Defense Advanced Research Projects Agency Young Faculty Award in 2008, the H. I. Romnes Faculty Fellowship of the University of Wisconsin–Madison in 2011, the National Institutes of Health Director's New Innovator Award in 2011, the Vilas Associate Award of the University of Wisconsin in 2013, and the Research to Prevent Blindness Stein Innovation Award in 2016.